



**A low-temperature route for producing epitaxial perovskite superstructures on (001)-oriented SrTiO<sub>3</sub>/Si substrates**

Journal:	<i>Journal of Materials Chemistry C</i>
Manuscript ID	TC-ART-04-2021-001988.R1
Article Type:	Paper
Date Submitted by the Author:	18-Jun-2021
Complete List of Authors:	Plokhikh, Aleksandr; Drexel University, Materials Science + Engineering Golovina, Iryna; Drexel University, Materials Science + Engineering Falmbigl, Matthias; Institute of Physical Chemistry, University of Vienna Karateev, Igor; Kurchatov Institute Vasiliev, Alexander; Russian Research Centre "Kurchatov Institute", NBIC Lapano, Jason; Pennsylvania State University Engel-Herbert, Roman; Pennsylvania State University Spanier, Jonathan; Drexel University, Materials Science + Engineering

## A low-temperature route for producing epitaxial perovskite superlattice structures on (001)-oriented SrTiO<sub>3</sub>/Si substrates

Aleksandr V. Plokhikh,<sup>1,\*</sup> Iryna S. Golovina,<sup>1,\*</sup> Matthias Falmbigl,<sup>1</sup> Igor A. Karateev,<sup>2</sup> Alexander L. Vasiliev,<sup>2,3</sup> Jason Lapano,<sup>4</sup> Roman Engel-Herbert,<sup>4,5,6</sup> and Jonathan E. Spanier<sup>1,7,8</sup>

<sup>1</sup>*Department of Materials Science & Engineering, Drexel University, Philadelphia, Pennsylvania 19104, USA*

<sup>2</sup>*National Research Center “Kurchatov Institute”, Kurchatov Square 1, Moscow 123182, Russia*

<sup>3</sup>*Moscow Institute of Physics and Technology (State University), MIPT, 9 Institutskiy per., Dolgoprudny, 141701 Moscow Region, Russia*

<sup>4</sup>*Department of Materials Science & Engineering, Pennsylvania State University, University Park, Pennsylvania 16802, USA*

<sup>5</sup>*Department of Chemistry, Pennsylvania State University, University Park, Pennsylvania 16802, USA*

<sup>6</sup>*Department of Physics, Pennsylvania State University, University Park, Pennsylvania 16802, USA*

<sup>7</sup>*Department of Mechanical Engineering and Mechanics, Drexel University, Philadelphia, Pennsylvania 19104, USA*

<sup>8</sup>*Department of Physics, Drexel University, Philadelphia, Pennsylvania 19104, USA*

\* Authors with equal contribution

### ABSTRACT

We report on the formation of epitaxial perovskite oxide superlattice structures by atomic layer deposition (ALD), which are integrated monolithically on Si wafers using a template layer of SrTiO<sub>3</sub> deposited by hybrid molecular beam epitaxy. ALD film growth was carried out at 360 °C, which is significantly lower than typical deposition temperatures for epitaxial perovskite thin films. The high control over the stacking sequence of different constituents is demonstrated in a series of (BaTiO<sub>3</sub>)<sub>m</sub>/(SrTiO<sub>3</sub>)<sub>n</sub> superlattices with various *m/n* cycle ratios. All superlattice structures were coherently strained to the virtual substrate layer of SrTiO<sub>3</sub> on Si. Irrespective of *m/n* superlattice sequence, SrTiO<sub>3</sub> sublayers retain slight compressive strain which is transmitted to the BaTiO<sub>3</sub> layers.

## INTRODUCTION

For epitaxial individual perovskite oxides and hetero- or superlattice structures composed of two or more ternary oxides, pulsed laser deposition (PLD),<sup>1-3</sup> molecular beam epitaxy (MBE)<sup>4-6</sup> and metal-organic chemical vapor deposition (MOCVD)<sup>7,8</sup> techniques are currently successfully employed. The growth temperatures for the films utilizing these methods vary from 600°C (in MBE)<sup>4-6</sup> to 840°C (in PLD)<sup>1-3</sup>. A seamless integration into thin film fabrication technology of existing semiconductor industry complementary metal-oxide-semiconductor (CMOS) platforms is highly desirable. Although epitaxial films of exceptional quality can be fabricated using these techniques, the high deposition temperatures render these approaches inherently incompatible with, *e.g.*, back-end-of-line processing. Thus, a significant reduction of the growth temperature is paramount.

Atomic layer deposition (ALD) is a powerful technique with the capability of addressing this and related challenges due to a unique combination of arbitrary scalability, conformal coating, and low deposition temperatures.<sup>9,10</sup> A number of ALD process strategies have been developed to produce functional perovskite oxides, *e.g.*, BaTiO<sub>3</sub> and SrTiO<sub>3</sub>, with improved properties.<sup>11</sup> In particular, a thin (3-5 nm thick) SrTiO<sub>3</sub> seed layer was used to obtain the following main crystalline SrTiO<sub>3</sub> film with subsequent annealing at a higher temperature or without it.<sup>12-14</sup> This approach has resulted in enhanced electrical properties of SrTiO<sub>3</sub> films for dynamic random access memory (DRAM) applications. Recent studies showed that thin crystalline ternary *ABO*<sub>3</sub> perovskite oxides can be successfully integrated epitaxially on semiconductor substrates (Si, Ge, or GaAs) using ALD.<sup>15</sup> For a direct integration on a Si(001) substrate, a thin buffer layer of SrTiO<sub>3</sub> grown by the hybrid molecular beam epitaxy (hMBE) technique is used. The use of MBE grown SrTiO<sub>3</sub> as a viable template for incorporating other epitaxial oxide films onto Si is now ubiquitous.<sup>16-19</sup> Until now, a few functional perovskite oxides, such as BaTiO<sub>3</sub>,<sup>20</sup> SrTiO<sub>3</sub>,<sup>21</sup> BiFeO<sub>3</sub>,<sup>22</sup> and LaAlO<sub>3</sub>,<sup>23</sup> were deposited epitaxially on SrTiO<sub>3</sub>-buffered Si(001) substrates using ALD. While BaTiO<sub>3</sub> and SrTiO<sub>3</sub> films were crystalline as-deposited, BiFeO<sub>3</sub> and LaAlO<sub>3</sub> films were amorphous and required postdeposition anneals to crystallize at 450 °C and 600°C, respectively.<sup>22,23</sup> The post-deposition processing at relatively high temperatures forfeits the low deposition temperatures of ALD. Therefore, identifying strategies to obtain crystalline films by ALD directly during the deposition process remains important.

The direct formation of the crystalline complex (in particular, ternary) oxides using ALD has proved challenging.<sup>15,24-26</sup> Precursor structure (e.g., the sizes of the precursors) and the binary subcycles arrangement are considered the main driving forces that enable to facilitate the direct epitaxy by ALD.<sup>25,26</sup> Also, the technological factors that promote the direct epitaxy are growth rate, growth temperature, thermodynamic stability between the film and the substrate and epitaxial stabilization by minimal lattice mismatch.<sup>27</sup> Although the presence of a SrTiO<sub>3</sub> template layer on Si substrates can facilitate nucleation of a crystalline phase at low temperatures, it is insufficient in some other cases. Here, the role of the interface strain has not been clarified yet. While crystalline BaTiO<sub>3</sub> and SrTiO<sub>3</sub> films can be deposited at temperatures as low as 225 °C for the case of BaTiO<sub>3</sub><sup>20</sup> and 250 °C for the case of SrTiO<sub>3</sub><sup>21</sup>, the crystallization of Ba<sub>x</sub>Sr<sub>1-x</sub>TiO<sub>3</sub> solid solution with lattice parameters between the end members BaTiO<sub>3</sub> and SrTiO<sub>3</sub>, should be possible without additional annealing. Instead, *in situ* low temperature crystallization of Ba<sub>x</sub>Sr<sub>1-x</sub>TiO<sub>3</sub> is challenging using ALD due to the layered character of growth, which prevents the formation of solid solutions, and typically requires additional high-temperature *ex situ* annealing.<sup>28</sup> While the fact that BaO has a limited ALD growth rate on top of SrO plays a negative role in the deposition of Ba<sub>x</sub>Sr<sub>1-x</sub>TiO<sub>3</sub> films, the growth of a BaTiO<sub>3</sub>/SrTiO<sub>3</sub> superlattice structure provides an opportunity to overcome these roadblocks for low temperature ALD processing. The growth of epitaxial BaTiO<sub>3</sub>/SrTiO<sub>3</sub> superlattices on SrTiO<sub>3</sub>/Si virtual substrates has not been demonstrated so far, while numerous works have been done on BaTiO<sub>3</sub>/SrTiO<sub>3</sub> superlattice structures on Pt/SiO<sub>2</sub>/Si,<sup>29,30</sup> on TiN buffer layers on Si<sup>31</sup> or directly on SrTiO<sub>3</sub> substrates<sup>3,32-34</sup>. However, in all these cases, high-temperature deposition techniques such as PLD or MBE were used.

Here we demonstrate, for the first time, epitaxial (BaTiO<sub>3</sub>)<sub>m</sub>/(SrTiO<sub>3</sub>)<sub>n</sub> superlattice structures on (001)-oriented SrTiO<sub>3</sub>/Si substrates grown by ALD at a temperature of only 360 °C. This growth temperature for BaTiO<sub>3</sub>/SrTiO<sub>3</sub> superlattices is 400°C lower than the typical deposition temperatures utilized in PLD, MBE, and MOCVD, and well within the range for CMOS-compatible processes. Our approach unambiguously demonstrates the possibility to obtain epitaxial (BaTiO<sub>3</sub>)<sub>m</sub>/(SrTiO<sub>3</sub>)<sub>n</sub> superlattice structures with various *m/n* cycle ratios on Si substrates by using ALD on hMBE-grown SrTiO<sub>3</sub> buffer layers, at a substantially reduced growth temperature.

## I. EXPERIMENTAL SECTION

The metamorphic 18-nm-thick (001)-oriented SrTiO<sub>3</sub> buffer layer was grown using hMBE described in detail elsewhere.<sup>35-37</sup> The growth of the SrTiO<sub>3</sub> layer was conducted in two steps. First, a 10 monolayer thick template of SrTiO<sub>3</sub> is deposited on an etched (001)-oriented Si substrate at low temperatures (400-600 °C) by co-supplying elemental Sr and the organometallic Ti-precursor, titanium tetra-isopropoxide (TTIP), from a conventional effusion cell and gas injector, respectively. This initial deposition step was performed in the absence of additional oxygen. The Ti in the TTIP molecule is tetrahedrally coordinated by oxygen, which facilitates the formation of SrTiO<sub>3</sub> on the templated Si surface without forming an amorphous silicon dioxide layer at the interface. After the initial layer formation, growth rates and temperatures were increased to about 50 nm/hr at 600-900 °C until a total SrTiO<sub>3</sub> layer thickness of 18 nm was reached.

Atomic layer depositions of the BaTiO<sub>3</sub>/SrTiO<sub>3</sub> superstructures were conducted in a Picosun R200 Advanced Reactor. The reactor temperature was maintained at 360 °C, and the base pressure was ~10 hPa. using Absolut Ba (Air Liquide, Ba(iPr<sub>3</sub>Cp)<sub>2</sub>), Absolut Sr (Air Liquide, Sr(iPr<sub>3</sub>Cp)<sub>2</sub>), Ti-tetramethoxide (Alfa Aesar Ti(OMe)<sub>4</sub>, TMO) as cation precursors and O<sub>3</sub> as oxidizer were used. High purity N<sub>2</sub> (Airgas, 99.9999 %) was used as carrier gas. The pulse and purge times were 1.6/6 s for Ba(iPr<sub>3</sub>Cp)<sub>2</sub> and Sr(iPr<sub>3</sub>Cp)<sub>2</sub>, 0.1/3 s for TMO, and 0.4/3 s for O<sub>3</sub>, respectively. The pulse sequences for the BaTiO<sub>3</sub> and SrTiO<sub>3</sub> subcycles were 2×(Ba(iPr<sub>3</sub>Cp)<sub>2</sub>/Sr(iPr<sub>3</sub>Cp)<sub>2</sub> + O<sub>3</sub>): 3×(TMO + O<sub>3</sub>) providing a 1:1 cation ratio for each individual ternary perovskite film. While it was already demonstrated that Sr(iPr<sub>3</sub>Cp)<sub>2</sub> is stable at this deposition temperature, the self-decomposition of Ba(iPr<sub>3</sub>Cp)<sub>2</sub> and TMO has negligible contribution to the total growth rate, respectively, as was shown in our previous papers.<sup>38-40</sup> A set of films with various cycle ratios  $m/n = 1/5, 3/5, 5/5, 5/3$  and  $5/1$  was produced and characterized using X-ray diffraction (XRD), scanning electron microscopy (SEM), high resolution transmission electron microscopy (HR-TEM) and scanning transmission electron microscopy (STEM) and X-ray photoelectron spectroscopy (XPS).

XRD scans were performed on a Rigaku Smartlab using Cu-K<sub>α1</sub> radiation. The film composition was measured using a Zeiss Supra 50 VP Scanning Electron Microscope equipped with an energy-dispersive detector (Oxford Instruments) on Si-wafers. A reciprocal space map (RSM) was collected on a Bruker D8 Discovery diffractometer using a Cu-K<sub>α</sub> source and a Ge (220) double bounce monochromator. The scan was collected using a 1D detector (LYNXEYE) in 1D mode with a width of 2.7°.

Cross-sections of the thin film samples for high resolution transmission electron microscopy (HR-TEM) and scanning transmission electron microscopy (STEM) were prepared in a Helios Nanolab 600i (FEI, USA) Scanning Electron Microscope (SEM)/Focused Ion Beam (FIB) dual beam system equipped with gas injectors for W and Pt deposition and an Omniprobe micromanipulator (Omniprobe, USA). After depositing a 2  $\mu\text{m}$  thick protective Pt layer, milling using a 30 keV  $\text{Ga}^+$  ion beam resulted in a cross-section area of  $5 \times 5 \mu\text{m}^2$ , which was subsequently polished with 5 keV and 2 keV  $\text{Ga}^+$  ion beams, respectively. These cross sections were investigated utilizing a Titan 80–300 operated at 300 kV, which is equipped with a high-angle annular dark-field (HAADF) detector (Fischione, USA), a spherical aberration ( $C_s$ ) probe corrector and a post-column Gatan image filter (GIF). Digital Micrograph (Gatan, USA) and Tecnai Imaging and Analysis (FEI, USA) software were used for the image processing.

XPS measurements were conducted using a Physical Electronics VersaProbe 5000 under a base-pressure of  $\sim 10^{-6}$  Pa. An Al- $K_{\alpha}$  source provided incident photons with an energy of 1486.6 eV at 10 kW  $\text{mm}^{-2}$ . The XPS spectra were collected with the pass energy of 23 eV. An electron neutralizer was used to neutralize the surface. Linear energy correction was applied in reference to the carbon spectra. The energy of the C1s peak of non-oxidized carbon was set at 284.8 eV. The detector was placed at the shallow angle of  $5^\circ$  relative to the plane of film surface. In order to measure a depth profile of the film, fast XPS-measurements were performed between  $\text{Ar}^+$  ion sputtering steps. The  $\text{Ar}^+$  ion sputtering process was conducted at an acceleration voltage of 1 kV and an ion current of 1  $\mu\text{A}$  per  $2 \times 2 \text{ mm}^2$  area at  $45^\circ$  in order to provide controllable and stoichiometric sputtering. The total duration of all sputtering steps was 12 sec. XPS spectra for Ba3d, Sr3d, C1s, O1s, and Si2p bands were collected as the most intensive lines for the Ba, Sr, C, O, and Si respectively. All quantification and spectrum fittings were performed with Casa XPS software using a Shirley-type background.

## II. RESULTS AND DISCUSSION

In the first step of developing an ALD-process for the growth of  $\text{BaTiO}_3/\text{SrTiO}_3$  superlattices (SL), the ternary oxides,  $\text{BaTiO}_3$  and  $\text{SrTiO}_3$ , were deposited individually under similar growth conditions. Initially, the pulse ratios were adjusted with the smallest possible repeat numbers of (Ba/Sr)-O and Ti-O to provide stoichiometric cation ratios and thorough intermixing of the cations, which should facilitate the crystallization of ternary perovskite structures at low temperatures. The

growth rates for both constituents were measured individually, providing an average growth per ternary cycle (GPC) of 0.58 nm for BaTiO<sub>3</sub> and 0.46 nm for SrTiO<sub>3</sub>, respectively (see Experimental section for details). Subsequently, the sub-cycles for BaTiO<sub>3</sub> and SrTiO<sub>3</sub> were combined in different ratios for each constituent and repeated until a film thickness of ~40 nm was reached. We use the notation  $(m/n) \times p$ , where  $m$  and  $n$  denote the number of consecutive BaTiO<sub>3</sub> and SrTiO<sub>3</sub>-cycles (not the number of unit cells) and  $p$  is the number of total repeats.

The XRD patterns of 3 films after deposition at 360 °C are shown in Fig. 1. Remarkably, all patterns reveal high intensity SL(00 $l$ ) peaks from the films in the vicinity of the (00 $l$ )-reflections from the hMBE-grown 18 nm thick SrTiO<sub>3</sub> buffer layer after the deposition, indicating crystalline and highly oriented ALD films for all selected deposition sequences. A closer inspection of the XRD patterns unravels satellite peaks of the first order, SL(-1) and SL(1), arising from the artificial superlattice structure of alternating BaTiO<sub>3</sub> and SrTiO<sub>3</sub> layers. While these satellite peaks are not as prominent and continuous as for BaTiO<sub>3</sub>/SrTiO<sub>3</sub> superlattices with precisely controlled repeat unit thicknesses and abrupt interfaces, they clearly indicate the presence of Ba-rich and Sr-rich alternating layers within the films and can be indexed to the superlattice repeat unit thickness (see Fig. 1b and Table 1).<sup>41</sup> We further notice that main SL(00 $l$ ) peaks of the (BaTiO<sub>3</sub>) <sub>$m$</sub> /(SrTiO<sub>3</sub>) <sub>$n$</sub>  superlattice structure shift to the lower  $2\Theta$  angle, while becoming narrower and higher in intensity as the content of BaTiO<sub>3</sub> increases in the film.

Calculating the  $c$ -lattice parameter from the  $2\Theta$  positions of the main diffraction peaks SL(00 $l$ ) for each (BaTiO<sub>3</sub>) <sub>$m$</sub> /(SrTiO<sub>3</sub>) <sub>$n$</sub>  superlattice structure results in a range from 3.97 Å to 4.01 Å increasing with the fraction of BaTiO<sub>3</sub> (Table 1 and Fig. S2). Note that the cubic lattice parameters of the ternary end members are:  $a = 3.905$  Å for SrTiO<sub>3</sub> and  $a_{\text{PC}} = 4.01$  Å for BaTiO<sub>3</sub>. The values for the average  $c$ -lattice parameters of the superlattice structures should represent the average thickness for both constituents and are slightly larger than the expected average value calculated from the end members. This difference is attributed to the presence of the compressive strain imparted by the hMBE grown SrTiO<sub>3</sub> layer onto the ALD-grown BaTiO<sub>3</sub>-layers.

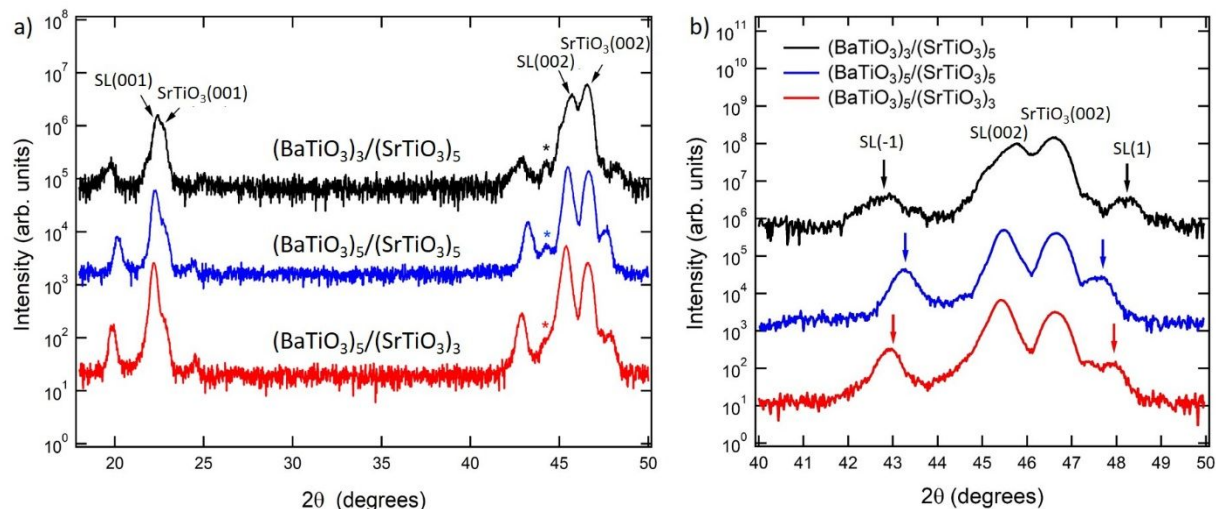


**Figure 1. a)** X-ray diffraction of 3  $(\text{BaTiO}_3)_m/(\text{SrTiO}_3)_n$  superlattice films with varying  $m/n$  pulse cycle ratios. The stage peak at  $\sim 44.3^\circ$  is marked with asterisks. **b)** Enlarged range around the (002)- $\text{SrTiO}_3$  substrate peak. The first-order SL(-1) and SL(1) satellite peaks marked with an arrow indicate the diffraction maxima from the superlattice repeat units. The stage peak is omitted in b) by using a Si-wafer below the sample.

**Table 1.** Series of 3 superlattices  $((\text{BaTiO}_3)_m/(\text{SrTiO}_3)_n) \times p$  with varying  $(m/n) \times p$  cycle numbers,  $c$ -lattice parameter calculated for the main peak, superlattice repeat unit thickness, and total film thickness.

$(m/n) \times p$	$c$ -lattice parameter, Å	Superlattice thickness, Å	Total film thickness, Å
$(3/5) \times 10$	3.97	39.8	406
$(5/5) \times 8$	3.99	47.9	388
$(5/3) \times 10$	4.01	40.0	375

The segregation into Ba-rich and Sr-rich layers in a periodic sequence is further corroborated by an XPS depth profile using Ar-ion sputtering (Fig. 2). Here, a clear oscillation of the Ba/Sr ratio is observed, while the Ti- and O-content exhibit only minor modulations throughout the superlattice structure. The 6 maxima/minima in the Ba/Sr-ratio are consistent with the deposition sequence for a  $(\text{BaTiO}_3)_5/(\text{SrTiO}_3)_5 \times 6$  superlattice. The total sputtering rate was  $\sim 3$  nm/min.

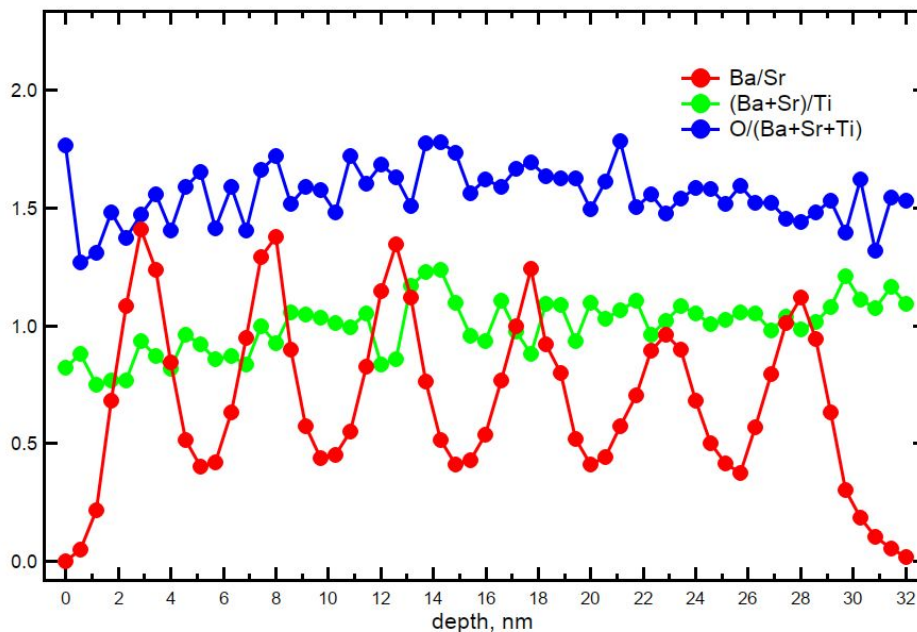


**Figure 2.** XPS depth profile for a  $(\text{BaTiO}_3)_5/(\text{SrTiO}_3)_5$  superlattice with a total number of 6 repeat units and a film thickness of 32 nm.

High angle angular dark field (HAADF) STEM images of an exemplary  $(\text{BaTiO}_3)_5/(\text{SrTiO}_3)_5$  superlattice structure with a total of 8 repeats are shown in Fig. 3. A cross-sectional image (Fig. 3, left) shows the entire layered structure over a large length scale with 8 repeat units of alternating bright ( $\text{BaTiO}_3$ ) and dark ( $\text{SrTiO}_3$ ) layers on the virtual (001)-oriented  $\text{SrTiO}_3/\text{Si}$ -substrate. A closer inspection at higher magnification (Fig. 3, right) unravels fully crystalline layers. However, the interfaces between the  $\text{BaTiO}_3$  and  $\text{SrTiO}_3$  layers are not atomically sharp, but exhibit a wave-like appearance. The interface modulation is on average 1–2-unit cells and stretched laterally over 8–10-unit cells. Unlike superlattice structures grown by high temperature methods, which typically exhibit atomically sharp interfaces due to a unit cell by unit cell growth mode, the ALD-grown superlattice structures show this unique feature. The waviness most likely arises from the growth method, which is not providing the exact amount of atoms per pulse to enable a layer-by-layer growth, but supplies a stoichiometric amount of cations within each subcycle. Evidence for this fundamental difference is provided by the average thickness of 0.58 nm/ $\text{BaTiO}_3$ - and 0.46 nm/ $\text{SrTiO}_3$ -subcycle, which do not correspond to the unit cell thicknesses.

HAADF STEM images of the  $(\text{BaTiO}_3)_3/(\text{SrTiO}_3)_5$  and  $(\text{BaTiO}_3)_5/(\text{SrTiO}_3)_3$  superlattices with a total of 10 repeats are shown in Fig. 4. For each superlattice, a fully crystalline film with alternating  $\text{BaTiO}_3$  and  $\text{SrTiO}_3$  sublayers was observed. Interestingly the  $(\text{BaTiO}_3)_m/(\text{SrTiO}_3)_n$  superlattices with  $m/n=1/5$  and  $5/1$ , although exhibiting initial epitaxy, were only partially crystallized. Amorphous areas form after first 4 repeats in the  $(\text{BaTiO}_3)_1/(\text{SrTiO}_3)_5$  superlattice and even sooner, practically during the first repeat, in the  $(\text{BaTiO}_3)_5/(\text{SrTiO}_3)_1$  superlattice. Corresponding HAADF STEM images of  $(\text{BaTiO}_3)_1/(\text{SrTiO}_3)_5$  and  $(\text{BaTiO}_3)_5/(\text{SrTiO}_3)_1$  superlattice structures with a total number of 10 repeats are shown in Fig. S3. This result may indicate that a too thin  $\text{BaTiO}_3$  or  $\text{SrTiO}_3$  sublayer cannot produce a stable nucleus of a new phase for sequential growth and therefore interrupts the growth front by forming an amorphous layer. Another possible explanation is that the crystalline layer does not form due to low-temperature kinetic limitations on the path of formation of a semi-coherent interface with the sublayer.<sup>27</sup> Several other factors and mechanisms can contribute to this behavior, such as a slight off-stoichiometry of one of the constituents<sup>15,42</sup> or preferred nucleation on defect sites.<sup>15,24</sup>

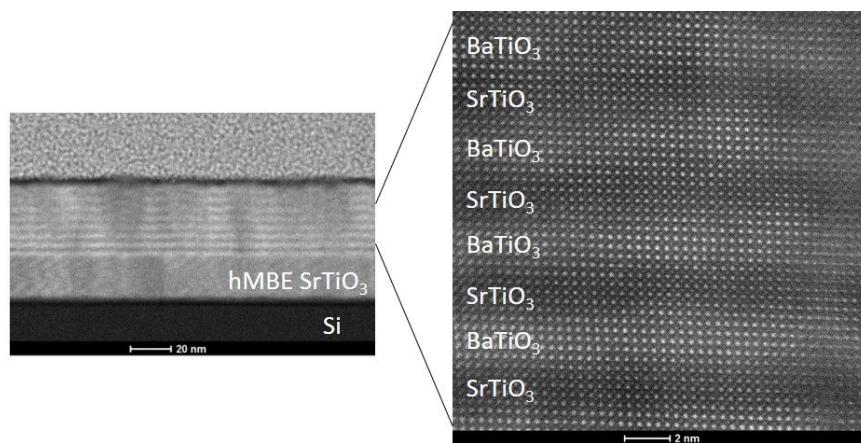


**Figure 3.** High angle angular dark field scanning transmission electron microscopy images of a  $(\text{BaTiO}_3)_5/(\text{SrTiO}_3)_5$  superlattice with a total number of 8 repeats.

Selected area electron diffraction (SAED) with representative indexed reflections for a  $(\text{BaTiO}_3)_5/(\text{SrTiO}_3)_5$  superlattice is presented in Fig. 5 and shows a prominent splitting of  $(00l)$  reflections of the superlattice (SL) structure from the hMBE- $\text{SrTiO}_3$  buffer layer peaks due to the difference in the out-of-plane parameters. By contrast, the in-plane  $(0k0)$  reflections do not show any splitting and confirm the epitaxial integration of the  $\text{SrTiO}_3$  buffer layer with the superlattice

structure, which by itself consists of epitaxially integrated layers. SAED images taken from the  $(\text{BaTiO}_3)_3/(\text{SrTiO}_3)_5$  and  $(\text{BaTiO}_3)_5/(\text{SrTiO}_3)_3$  superlattices with partial indexation of the SAED image for a  $(\text{BaTiO}_3)_5/(\text{SrTiO}_3)_3$  superlattice are shown in Figs. S4 and S5. An enlarged view of the higher order 00-4 reflections displayed in the top-right corner of Fig. 5 demonstrates the most prominent splitting of 00-4 reflections of superlattice structure and  $\text{SrTiO}_3$  buffer layer. The intensity diagram of this area further unravels additional satellite peaks from the superlattice structure SL(-1). The blue arrow in the enlarged view corresponds to the position axis in the intensity diagram.

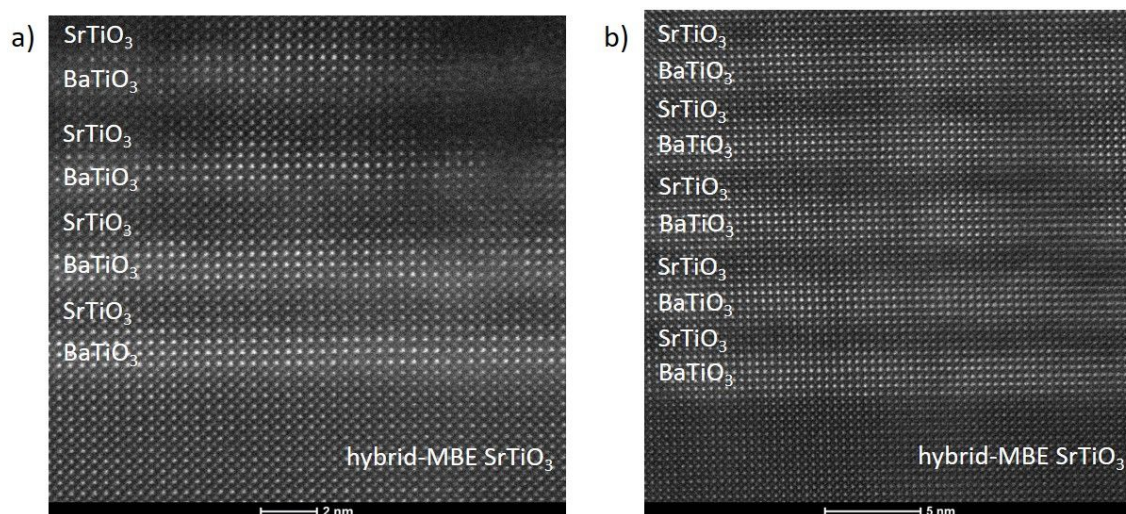


**Figure 4.** HAADF STEM images of a)  $(\text{BaTiO}_3)_3/(\text{SrTiO}_3)_5$  and b)  $(\text{BaTiO}_3)_5/(\text{SrTiO}_3)_3$  superlattices having a total number of 10 repeats.

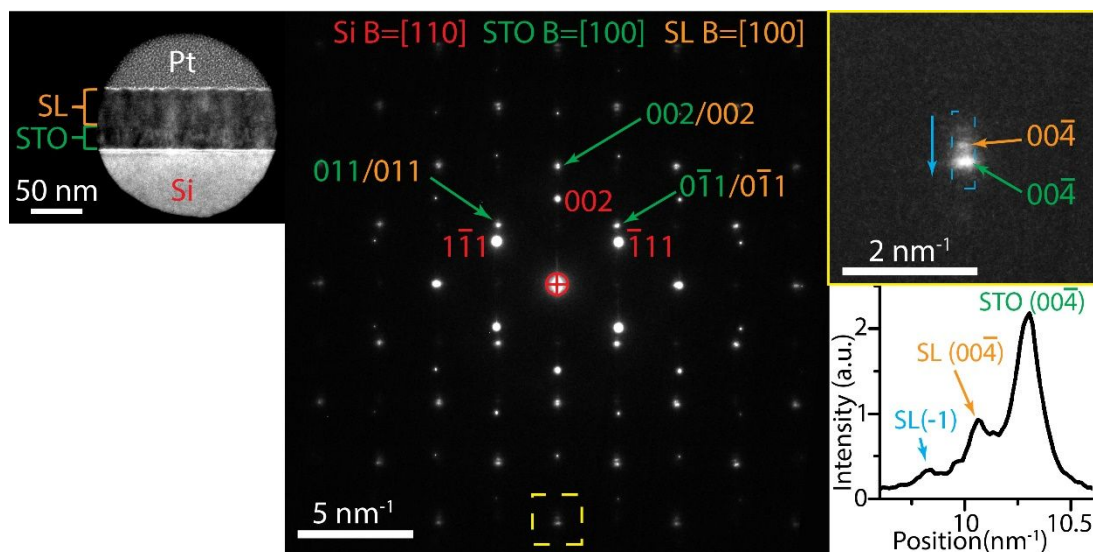


**Figure 5.** Electron diffraction image taken on a  $(\text{BaTiO}_3)_5/(\text{SrTiO}_3)_5$  superlattice structure from the area shown in the inset in the top-left corner. The small orange box highlights the area of higher order 00-4 reflections, which shows the most prominent splitting of superlattice (SL) and  $\text{SrTiO}_3$  buffer layer. The inset (large orange box in the top-right corner) is an enlarged view of this area. The blue arrow in the enlarged view corresponds to the position axis of the intensity diagram displayed in the bottom-right corner.

The  $a$ - and  $c$ -lattice parameters calculated from the SAED and STEM images for each  $(\text{BaTiO}_3)_m/(\text{SrTiO}_3)_n$  superlattice are summarized in Table 2. Since electron diffraction patterns show reflections from the superlattice structure (*e.g.*, SL(00-4) and satellite SL(-1) peaks in Fig. 5), and not from  $\text{BaTiO}_3$  and  $\text{SrTiO}_3$  individual layers, only average  $a$ - and  $c$ -lattice parameters of the films can be obtained from SAED images. We notice a good agreement between average  $c$ -parameters obtained from SAED and those obtained from XRD data (see Table 1) for a series of three  $(\text{BaTiO}_3)_m/(\text{SrTiO}_3)_n$  superlattices. Meanwhile, from STEM images in-plane  $a$ -lattice parameter and out-of-plane  $c$ -lattice parameter for individual  $\text{BaTiO}_3$  and  $\text{SrTiO}_3$  layers can be directly measured. Here, the figure in parenthesis provides the so-called standard uncertainty or estimated standard deviation, which is frequently used to provide crystallographic information. In case of  $3.90(2)$  Å lattice parameter, it means  $3.90 \pm 0.02$  Å.

**Table 2.** In-plane *a*-lattice parameter and out-of-plane *c*-lattice parameter obtained from SAED and STEM images for a series of three  $(\text{BaTiO}_3)_m/(\text{SrTiO}_3)_n$  superlattices.

<i>m/n</i>	SAED average film parameters <i>a</i> -lattice parameter, Å <i>c</i> -lattice parameter, Å	STEM	
		<i>a</i> -lattice parameter, Å*	<i>c</i> -lattice parameter, Å*
		BaTiO <sub>3</sub>	SrTiO <sub>3</sub>
<b>3/5</b>	3.90(3)	3.89(3)	3.90(2)
	3.97(3)	4.06(3)	3.93(2)
<b>5/5</b>	3.90(3)	3.90(2)	3.90(2)
	3.99(3)	4.07(5)	3.90(3)
<b>5/3</b>	3.90(3)	3.89(2)	3.90(2)
	3.99(3)	4.02(3)	3.91(3)

\* Standard uncertainties are given in parentheses.

Phi-scans of SrTiO<sub>3</sub>(103), BaTiO<sub>3</sub>(103) and Si(404) planes are presented in Fig. 6. Reflections from SrTiO<sub>3</sub>(103) and BaTiO<sub>3</sub>(103) are aligned to each other and appear as series of four distinct peaks with comparable intensities and spaced by 90°. The Phi-scan of Si(404) plane has its own series of four equal-spaced reflections, which are shifted 45° relative to the series of SrTiO<sub>3</sub> (103) and BaTiO<sub>3</sub> (103) peaks. This data indicates that all layers in the superlattice structure are in macroscopic epitaxial registration with the Si substrate and to each other. The RSM results for the  $(\text{BaTiO}_3)_5/(\text{SrTiO}_3)_5$  superlattice (Fig. S6) for the (103) peak around the SrTiO<sub>3</sub>-buffered substrate layer indicate that the superstructure is fully strained to the crystallization layer, corroborating the SAED analysis. This epitaxial registry to the substrate is very difficult to attain with the commonly used two-step deposition and post-annealing process for ALD-grown complex oxides due to the possible room for the homogeneous nucleation and grain growth in the amorphous film, which may lead to break of epitaxy in comparison to heterogeneous nucleation and growth as is the case of film growth with *in-situ* crystallization.

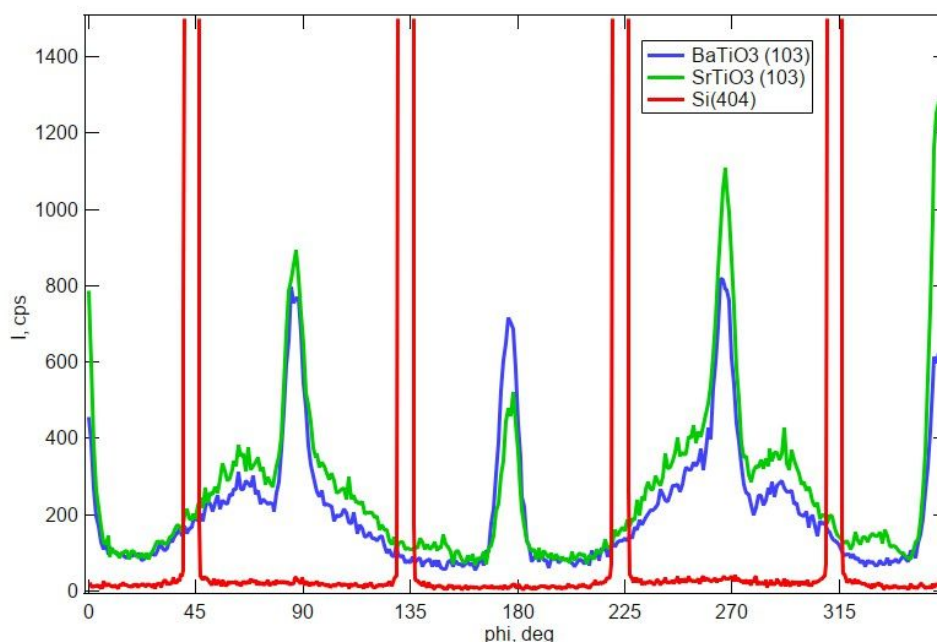


**Figure 6.** Phi-scans of SrTiO<sub>3</sub>(103), BaTiO<sub>3</sub>(103) and Si(404) planes of (BaTiO<sub>3</sub>)<sub>5</sub>/(SrTiO<sub>3</sub>)<sub>5</sub>/Si superstructure.

Interestingly, independent of the  $m/n$  ratio, the  $c$ -lattice parameter of the BaTiO<sub>3</sub> sublayer is larger than the  $a$ -lattice parameter, while both  $c$ - and  $a$ -lattice parameters of SrTiO<sub>3</sub> remain practically unchanged. These results reveal that the SrTiO<sub>3</sub> sublayer is almost unstrained, while BaTiO<sub>3</sub> is under compressive in-plane stress. Within the estimation error, the tetragonality of BaTiO<sub>3</sub> is  $c/a=1.044$  and practically identical for (BaTiO<sub>3</sub>)<sub>5</sub>/(SrTiO<sub>3</sub>)<sub>5</sub> and (BaTiO<sub>3</sub>)<sub>5</sub>/(SrTiO<sub>3</sub>)<sub>3</sub> superlattices, while it is a bit smaller, *i.e.*,  $c/a=1.033$ , for the (BaTiO<sub>3</sub>)<sub>3</sub>/(SrTiO<sub>3</sub>)<sub>5</sub> structure. Based on these results, the orientation of polarization in the BaTiO<sub>3</sub> layers and the strained state of the (BaTiO<sub>3</sub>) <sub>$m$</sub> /(SrTiO<sub>3</sub>) <sub>$n$</sub>  superlattice are represented in Fig. 7. The out-of-plane polarization orientation caused by in-plane compressive strain in the BaTiO<sub>3</sub> sublayers and practically unstrained state of the SrTiO<sub>3</sub> sublayers are consistent with theoretical studies<sup>43-45</sup> and experimental measurements of polarization and domain structure conducted for epitaxial (BaTiO<sub>3</sub>) <sub>$m$</sub> /(SrTiO<sub>3</sub>) <sub>$n$</sub>  superlattices obtained by MBE<sup>5,46,47</sup>, PLD<sup>48</sup>, and magnetron sputtering<sup>49</sup> techniques. Given the BaTiO<sub>3</sub> is a classical ferroelectric, the tetragonality and an increase of polarization along  $c$ -axis is expected in the BaTiO<sub>3</sub> sublayer. It is also predictable that SrTiO<sub>3</sub> being a paraelectric in bulk may remain cubic and unstrained in the SrTiO<sub>3</sub> sublayer. When the thickness of the individual constituent layers in the (BaTiO<sub>3</sub>) <sub>$m$</sub> /(SrTiO<sub>3</sub>) <sub>$n$</sub>  superlattice is only a few

unit cells ( $m=n=1-3$ ), the BaTiO<sub>3</sub> and SrTiO<sub>3</sub> sublayers are electrostatically coupled, and so SrTiO<sub>3</sub> layers become polarized.<sup>43</sup> At higher thickness ( $m=n=5-6$ ), the polarization remain confined within BaTiO<sub>3</sub> sublayers. As  $m/n$  increases, the remanent polarization increases due to the increase of  $c$ -lattice parameter of the BaTiO<sub>3</sub> layer.<sup>50</sup> Although the first-principles calculations reveal a tetragonality in the SrTiO<sub>3</sub> sublayer with  $c/a = 1.008$  for the (BaTiO<sub>3</sub>)<sub>6</sub>/(SrTiO<sub>3</sub>)<sub>5</sub> superlattice, the deviation of this  $c/a$  from  $c/a = 1$  is too small to be accurately resolved by HR-TEM.<sup>44</sup>

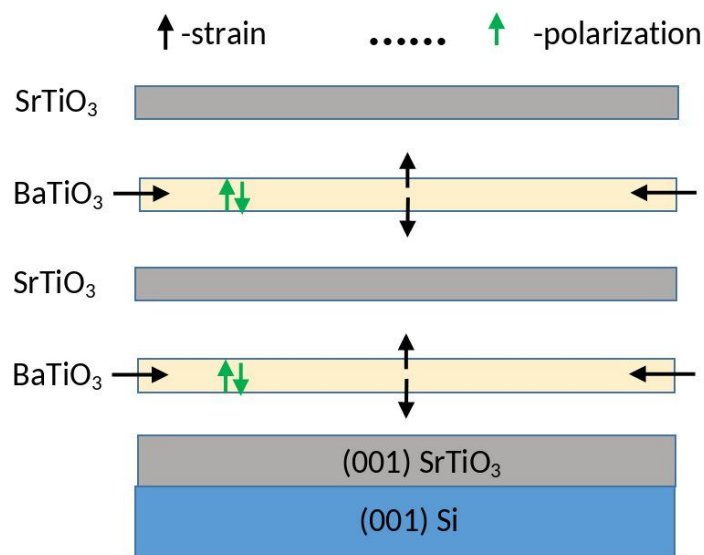


**Figure 7.** A schematic representation of a strained (BaTiO<sub>3</sub>)<sub>m</sub>/(SrTiO<sub>3</sub>)<sub>n</sub> superlattice grown by ALD. The out-of-plane polarization orientation and in-plane compressive strain in the BaTiO<sub>3</sub> layers are indicated by green and black arrows, respectively.

### III. CONCLUSIONS

Epitaxial  $\approx 40$ -nm-thick (BaTiO<sub>3</sub>)<sub>m</sub>/(SrTiO<sub>3</sub>)<sub>n</sub> superlattice structures with cycle ratios  $m/n = 1/3, 3/5, 5/5, 5/3$  and  $5/1$  were grown on (001)-oriented STO/Si substrates by ALD at a temperature of 360 °C, which is only roughly half as high as the growth temperatures conventionally used for BaTiO<sub>3</sub>/SrTiO<sub>3</sub> superlattices grown by PLD, MBE, or MOCVD. While (BaTiO<sub>3</sub>)<sub>3</sub>/(SrTiO<sub>3</sub>)<sub>5</sub>, (BaTiO<sub>3</sub>)<sub>5</sub>/(SrTiO<sub>3</sub>)<sub>5</sub> and (BaTiO<sub>3</sub>)<sub>5</sub>/(SrTiO<sub>3</sub>)<sub>3</sub> superlattices are almost fully crystalline, (BaTiO<sub>3</sub>)<sub>1</sub>/(SrTiO<sub>3</sub>)<sub>5</sub> and (BaTiO<sub>3</sub>)<sub>5</sub>/(SrTiO<sub>3</sub>)<sub>1</sub>, while exhibiting initial epitaxy, are only partially crystallized after 3-5 repeat supercycles. The HAADF STEM images show that interfaces between the BaTiO<sub>3</sub> and SrTiO<sub>3</sub> are not atomically smooth. The XRD phi-scan and RSM data reveal that

all films are coherently strained to the substrate. From STEM data, the out-of-plane  $c$ -lattice parameter and in-plane  $a$ -lattice parameter for individual  $\text{BaTiO}_3$  and  $\text{SrTiO}_3$  sublayers have been obtained. Independent of the  $m/n$  ratio,  $c$ -lattice parameters are larger than the  $a$ -lattice parameter of the  $\text{BaTiO}_3$  sublayer, while both  $c$ - and  $a$ -lattice parameters of  $\text{SrTiO}_3$  remain practically unchanged within the estimation error. Therefore,  $\text{SrTiO}_3$  sublayers are almost unstrained, while  $\text{BaTiO}_3$  sublayers are under compressive in-plane strain.

## SUPPLEMENTARY MATERIAL

Data on superlattice length and  $c$  lattice parameter, additional HAADF and SAED data, and RSM data.

## ACKNOWLEDGMENTS

The authors at Drexel University acknowledge support from the U.S. Army Research Laboratory under W911NF-19-2-0119, the Office of Naval Research under N00014-15-2170 and by the National Science Foundation under DMR 1608887. Jason Lapano and Roman Engel-Herbert acknowledge support from the National Science Foundation MRSEC Center for Nanoscale Science at Penn State through grant number DMR 1420620. Electron microscopy was conducted using the equipment of the Resource Center of Probe and Electron Microscopy (Kurchatov Complex of NBICS-Technologies, NRC “Kurchatov Institute”). The authors thank K. Chen and X. Xi for access to an X-ray diffractometer within the Temple Materials Institute at Temple University. The authors acknowledge the Materials Characterization Facilities at Drexel University for access to XRD (NSF DMR 1040166) and XPS (NSF CBET 0959361) and Picosun Oy (Finland) for assistance.

## References

1. M. Liu, C. Ma, G. Collins, J. Liu, C. Chen, A. D. Alemayehu, G. Subramanyam, Y. Ding, J. Chen, C. Dai, Y. Lin and M. W. Cole, *Nanoscale Research Letters*, 2013, **8**, 338.
2. H. Tabata, H. Tanaka and T. Kawai, *Appl. Phys. Lett.*, 1994, **65** (15), 1970-1972.

3. O. Nakagawara, T. Shimuta, T. Makino, S. Arai, H. Tabata and T. Kawai, *Appl. Phys. Lett.*, 2000, **77**, 3257–3259.
4. K. Kathan-Galipeau, P. P. Wu, Y. L. Li, L. Q. Chen, A. Soukiassian, Y. Zhu, D. A. Muller, X. X. Xi, D. G. Schlom and D. A. Bonnell, *J. Appl. Phys.* 2012, **112**, 052011.
5. D. G. Schlom, J. H. Haeni, J. Lettieri, C. D. Theis, W. Tian, J. C. Jiang and X. Q. Pan, *Mater. Sci. Eng. B*, 2001, **87**, 282-291.
6. T. Harigai, H. Kimbara, H. Kakemoto, S. Wada and T. Tsurumi, *Ferroelectrics*, 2007, **357**, 128–132.
7. F. Weiss, M. Audier, A. Bartaszyte, D. Bellet, C. Girardot, C. Jimenez, J. Kreisel,; S. Pignard, M. Salaun and C. Ternon, *Pure Appl. Chem.*, 2009, **81**, 1523–1534.
8. Z. Wang, S. Oda, M. Karlsteen, U. Sodervall and M. Willande, *Jpn. J. Appl. Phys.*, 2000, **39**, 4164–4167.
9. N. P. Dasgupta, H.-B.-R. Lee, S. F. Bent and P. S. Weiss, *Chem. Mater.*, 2016, **28**, 1943–1947.
10. H. H. Sønsteby, H. Fjellvåg and O. Nilsen, *Adv. Mater. Interfaces*, 2017, **4**, 1600903.
11. J. H. Shim, H. J. Choi, Y. Kim, J. Torgersen, J. An, M. H. Lee and F. B. Prinz, *J. Mater. Chem. C*, 2017, **5**, 8000-8013.
12. S. W. Lee, O. S. Kwon, J. H. Han and C. S. Hwang, *Appl. Phys. Lett.* 2008, **92**, 222903.
13. S. H. Kim, W. Lee, C. H. An, D.-G. Kim, D. S. Kwon, S. T. Cho, S. H. Cha, J. I. Lim and C. S. Hwang, *Phys. Stat. Sol. RRL* 2019, **13**, 1800557.
14. M. Popovici, K. Tomida, J. Swerts, P. Favia, A. Delabie, H. Bender, C. Adelman, H. Tielens, B. Brijs, B. Kaczer, M. A. Pawlak, M.-S. Kim, L. Altimime, S. Van Elshocht and J. A. Kittl, *Phys. Stat. Sol. (a)* 2011, **208**, 1920-1924.
15. M. D. McDaniel, T. Q. Ngo, S. Hu, A. Posadas, A. A. Demkov and J. G. Ekerdt, *Appl. Phys. Rev.*, 2015, **2**, 041301.
16. C. Dubourdieu, J. Bruley, T. M. Arruda, A. Posadas, J. Jordan-Sweet, M. M. Frank, E. Cartier, D. J. Frank, S. V. Kalinin, A. A. Demkov and V. Narayanan, *Nat. Nanotechnol.*, 2013, **8**, 748.
17. S. H. Baek, J. Park, D. M. Kim, V. A. Aksyuk, R. R. Das, S. D. Bu, D. A. Felker, J. Lettieri, V. Vaithyanathan, S. S. N. Bharadwaja, N. Bassiri-Gharb, Y. B. Chen, H. P. Sun, C. M. Folkman, H. W. Jang, D. J. Kreft, S. K. Streiffer, R. Ramesh, X. Q. Pan, S. Trolrier-

- McKinstry, D. G. Schlom, M. S. Rzechowski, R. H. Blick and C. B. Eom, *Science*, 2011, **334**, 958-961.
18. J. W. Park, D. F. Bogorin, C. Cen, D. A. Felker, Y. Zhang, C. T. Nelson, C. W. Bark, C. M. Folkman, X. Q. Pan, M. S. Rzechowski, J. Levy and C. B. Eom, *Nat. Commun.*, 2010, **1**, 94.
19. J. Wang, H. Zheng, Z. Ma, S. Prasertchoung, M. Wuttig, R. Droopad, J. Yu, K. Eisenbeiser and R. Ramesh, *Appl. Phys. Lett.*, 2004, **85**, 2574-2576.
20. T. Q. Ngo, A. B. Posadas, M. D. McDaniel, C. Hu, J. Bruley, E. T. Yu, A. A. Demkov and J. G. Ekerdt, *Applied Physics Letters*, 2014, **104**, 082910.
21. M. D. McDaniel, A. Posadas, T. Q. Ngo, A. Dhamdhere, D. J. Smith, A. A. Demkov and J. G. Ekerdt, *J. Vac. Sci. Technol.*, 2013, **A 31**, 01A136.
22. A. V. Plokhikh, I. A. Karataev, M. Falmbigl, A. L. Vasiliev, J. Lapano, R. Engel-Herbert and J. E. Spanier, *J. Phys. Chem. C*, 2019, **123**, 19, 12203-12210.
23. T. Q. Ngo, A. Posadas, M. D. McDaniel, D. A. Ferrer, J. Bruley, C. Breslin, A. A. Demkov and J. G. Ekerdt, *Journal of Crystal Growth*, 2013, **363**, 150–157.
24. H. H. Sønsteby, E. Skaar, Øy. S. Fjellvåg, J. E. Bratvold, H. Fjellvåg and O. Nilsen, *Nat. Commun.* 11, 2872 (2020).
25. H. H. Sønsteby, E. Skaar, H. Fjellvåg and O. Nilsen, *ACS Appl. Electron. Mater.* 2021, **3**, 292–298.
26. A. J. M. Mackus, J. R. Schneider, C. Macisaac, J. G. Baker and S. F. Bent, *Chem. Mater.* 2019, **31**, 1142–1183.
27. O. Yu. Gorbenko, S. V. Samoilenkov, I. E. Graboy and A. R. Kaul, *Chem. Mater.*, 2002, **14**, 10, 4026–4043.
28. T. T. Le and J. G. Ekerdt, *J. Vac. Sci. Technol. A*, 2020, **38**, 032401.
29. A. Sarkar and S. B. Krupanidhi, *J. Appl. Phys.*, 2007, **101**, 104113.
30. B. D. Qu, M. Evstigneev, D. J. Johnson and R. H. Prince, *Appl. Phys. Lett.*, 1998, **72**, 1394-1396.
31. T. U. Kim, B. R. Kim, W. J. Lee, J. H. Moon, B. T. Lee and J. H. Kim, *Journal of Crystal Growth*, 2006, **289**, 540-546.
32. T. Tsurumi, T. Ichikawa, T. Harigai, H. Kakemoto and S. Wada, *J. Appl. Phys.*, 2002, **91**, 2284 -2289.

33. A. Visinoiu, R. Scholz, S. Chattopadhyay, M. Alexe and D. Hesse, *Jpn. J. Appl. Phys.*, 2002, **41**, 6633–6638.
34. T. Shimuta, O. Nakagawara, T. Makino, S. Arai, H. Tabata T. Kawai, *J. Appl. Phys.*, 2002, **91**, 2290-2294.
35. L. Zhang and R. Engel-Herbert, *Phys. Status Solidi RRL*, 2014, **8**, 917-923.
36. M. Brahlek, A. S. Gupta, J. Lapano, J. Roth, H.-T. Zhang, L. Zhang, R. Haislmaier and R. Engel-Herbert, *Adv. Funct. Mater.*, 2017, **28**, 1702772.
37. L. Zhang, Y. Yuan, J. Lapano, M. Brahlek, S. Lei, B. Kabius, V. Gopalan and R. Engel-Herbert, Continuously Tuning Epitaxial Strains by Thermal Mismatch. *ACS Nano*, 2018, **12**, 1306–1312.
38. M. Falmbigl, I. S. Golovina, A. V. Plokhikh, D. Imbrenda, A. Podpirka, C. J. Hawley, G. Xiao., A. Gutierrez-Perez, I. A. Karataev, A. L. Vasiliev, T. C Parker and J. E. Spanier, *J. Phys. Chem. C.*, 2017, **121**, 16911–16920.
39. M. Falmbigl, I. A. Karateev, I. S. Golovina, A. V. Plokhikh, T. C. Parker, A. L. Vasiliev and J. E. Spanier, *Nanoscale* 2018, 10, 12515.
40. I. S. Golovina, M. Falmbigl, A. V. Plokhikh, A. L. Bennett-Jackson, A. J. Ruffino, A. D. Gutierrez-Perez, C. L. Johnson and J. E. Spanier, *Thin Solid Films*, 2020, **709**, 138123.
41. Z. Wang, S. Oda, M. Karlsteen, U. Sodervall and M Willander, *Jpn. J. Appl. Phys.* 2000, **39**, 4164–4167.
42. A. R. Akbashev, G. Chen and J. E. Spanier, *Nano Lett.* 2014, **14**, 44–49.
43. J. B. Neaton and K. M. Rabe, *Appl. Phys. Lett.*, 2003, **82**, 1586–1588.
44. W. Tian, J. C. Jiang, X. Q. Pan, J. H. Haeni, Y. L. Li, L. Q. Chen, D. G. Schlom, J. B. Neaton, K. M. Rabe and Q. X. Jia, *Appl. Phys. Lett.*, 2006, **89**, 23–25.
45. Y. L. Li, S. Y. Hu, D. Tenne, A. Soukiassian, D. G. Schlom, X. X. Xi, K. J. Choi, C. B. Eom, A. Saxena, T. Lookman, Q. X. Jia and L. Q. Chen, *Appl. Phys. Lett.*, 2007, **91**, 112914.
46. J. H. Haeni, C. D. Theis and D. G. Schlom, *J. Electroceram.* 2000, **4**, 385.
47. K. Kathan-Galipeau, P. Wu, Y. Li, L.-Q. Chen, A. Soukiassian, X. Xi, D. G. Schlom and D. A. Bonnell, *ACS Nano*, 2011, **5**, 640–646.
48. S. Estandía, F. Sánchez, M. F. Chisholm and J. Gázquez, *Nanoscale*, 2019, **11**, 21275.

49. B. Bein, H. C. Hsing, S. J. Callori, J. Sinsheimer, P. V. Chinta, R. L. Headrick and M. Dawber, *Nat. Commun.*, 2015, **6**, 10136.
50. T. Shimuta, O. Nakagawara, T. Makino, S. Arai, H. Tabata and T. Kawai, *J. Appl. Phys.*, 2002, **91**, 2290-2294.